IMECE2004-60060

DESIGN OF A SPATIAL LINKAGE HAPTIC INTERFACE

John Ryan Steger   Ronald M. Chung   Kevin Lin   H. Kazerooni

Department of Mechanical Engineering
University of California, Berkeley
Berkeley, CA 94720

ABSTRACT

This paper describes the mechanical and electrical design of a compact high fidelity desktop haptic interface that provides three-degree-of-freedom point-force interaction through a handheld pen-like stylus. The complete haptic device combines a spatial linkage, actuation, power amplification, and control electronics in a standalone package with a footprint similar to that of a notebook computer (33cm x 25cm x 10cm). The procedure used to design the statically balanced spatial linkage is explained and both an inexpensive lightweight plastic version and a high stiffness, high strength, aluminum and stainless steel version are presented. The theory and implementation of sinusoidal encoder interpolation and sinusoidal servo-motor commutation used to achieve high-fidelity haptic simulation is covered for two versions of electronic control hardware: custom hardware based on a digital signal processor (DSP) and an off-the-shelf design based on an embedded PC.

KEYWORDS

Haptic interface; spatial linkage; static balance; sinusoidal interpolation; sinusoidal commutation.

OBJECTIVE

Our goal was to create a portable self-contained haptic device for precision finger-scale interaction that could enable point force interaction over a three-dimensional translational work volume. The resulting device is a desktop unit intended to provide a haptic interface to PC based virtual environments (Fig. 1). Through the use of a unique kinematic linkage [1], we sought to create a haptic device with capabilities equal to or better than those of commercially available haptic interfaces.

Because the purpose of a haptic device is to simulate the forces generated through interaction with physical objects, performance is typically measured by the level of tactile realism achieved. Guidelines for obtaining a realistic haptic simulation include multiple degrees of freedom, human matched force capability, low friction, near-zero backlash, and gravitational counterbalancing [2]. The present joystick design addresses these points and offers exceptionally smooth force output, low inertia resulting in high motion bandwidth, and high motion resolution. Our design goal is to develop a single unit stand-alone desktop haptic interface device that combines high performance with portability and low manufacturing cost.

BACKGROUND

Through application of our patented kinematic linkage architecture [3], we sought to create a haptic device with capabilities comparable in many respects to those currently available in commercial haptic interfaces like the PHANToM Haptic Interface, produced by SensAble Technologies [4]. The performance specifications of the original PHANToM (Model: "Premium 1.0") set the following targets for realistic simulation of precision finger-scale manipulation: less than 0.1 N static back-drive friction, inertia such that the user perceives unbalanced weight of 0.2 N or less, maximum stiffness of 35 N/cm, peak and continuous end effector forces of 10 N and 1.5 N respectively, and end effector spatial resolution of at least 400 dpi (98 μm) [4]. Like many of its predecessors, the PHANToM makes use of serial linkage elements as part of the force transmitting mechanism. A purely serial mechanism employs a single path to connect its base link to its terminal link. In this configuration, proximal links (links closer to the base) in a chain are required to carry and move the more distal links (those closer to the end point) and their actuators, resulting in increased linkage inertia and decreased linkage stiffness.

Conversely, a parallel mechanism joins its base and terminal links across multiple pathways. In the case of our joystick, its links are arranged in a fully parallel mechanism that allows for the attachment of actuators to the ground, significantly reducing the system inertia. Moreover, because a

Copyright © 2004 by ASME
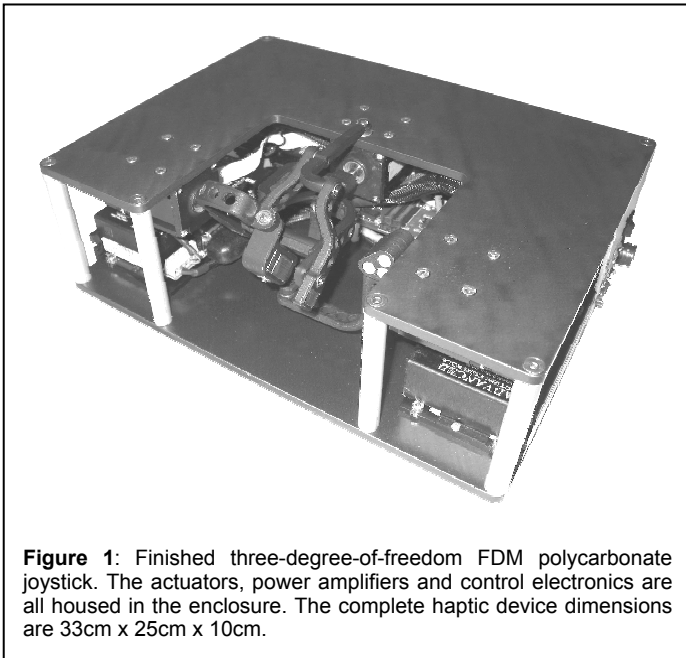
Figure 1: Finished three-degree-of-freedom FDM polycarbonate joystick. The actuators, power amplifiers and control electronics are all housed in the enclosure. The complete haptic device dimensions are 33cm x 25cm x 10cm.

parallel mechanism uses multiple pathways arranged in one or more closed kinematic loops, the resulting device can be made to have higher stiffness than serial mechanisms, which in turn allows for high bandwidth force transmission. Other haptic devices that make use of a parallel configuration include Gough-Stewart platform-like haptic devices [5-7], wire-actuated [8-10], and spherical mechanisms [11-13] similar to the scheme chosen for our design.

For several years, UC Berkeley and NASA Ames have collaborated on the development of joystick-type haptic devices based on a common underlying parallel planar-spherical spatial kinematic architecture [1]. The haptic devices described in this paper represents the most recent iterations of this research. The first joystick produced used a large set of links and provided for full arm-scale motion in the joystick workspace [12]. This device was later scaled down to provide a workspace compatible with the smaller finger and hand motions associated with using a writing instrument or a computer mouse [13]. The current joystick maintains the finger-motion-sized workspace of the previous device and improves both the joystick linkage design and the control hardware and software.

To achieve realistic haptic simulation, a tightly regulated, temporally deterministic response from the haptic interface is needed. We originally selected a Digital Signal Processor (DSP) based architecture allowing us to isolate time-critical haptic interface control tasks from computationally intensive and more slowly updated Virtual Environment (VE) simulation processes. The standalone DSP is embedded inside the haptic interface itself, maintaining portability by allowing the device to be connected with different VE simulation computers. A Field Programmable Gate Array (FPGA) was included to provide the high-speed dedicated I/O for reading haptic interface sensors and commanding actuators.

While the DSP/FPGA based design met the performance requirements, the custom control hardware was both expensive

to produce and did not provide the robustness necessary for regular experimental use. A second generation of control hardware was designed using only commercially available off-the-shelf components, allowing it to be assembled in prototype quantities quickly and inexpensively. This version is based on an embedded x86 microprocessor and a commercially available motion control processor. This new control electronics package maintains the portable self-contained overall design of the haptic device.

These joystick devices have been used in haptic demonstrations in our labs, including investigations of texture perception [12,14]. The new metal joystick described in this paper is intended for ongoing human performance research at NASA Ames.

DEVICE OVERVIEW

All versions of this haptic device share a common joystick linkage architecture (Fig. 2) that contains 10 rigid links with 12 revolute joints, in a parallel spherical mechanism arranged in three closed kinematic loops. The device provides point-force interaction over a three-dimensional translational work volume and has evolved from previous joysticks designed in our lab [1]. The joystick is manipulated through various styli that attach to a magnetic ball joint on the endpoint. The links are passively mass balanced so gravity forces cannot be sensed by the user as the end effector is moved.

Actively controlled force is provided by three brushless DC motors with housings fixed to the joystick enclosure so the linkage does not carry their weight. Open loop force and motion transfer fidelity is improved due to the lack of transmission elements such as gears or cable drives that would otherwise increase friction and add backlash. Sinusoidally wound, brushless DC motors are used, providing up to 5N of force at the joystick endpoint for short durations (2 sec, based on amplifier and motor specifications). Because sinusoidal motor commutation is matched to the motor winding profile, torque ripple—spatially dependent periodic deviations from commanded actuator torque—is eliminated, providing smooth feeling surfaces during joystick simulations. The use of analog sinusoidal encoders and sinusoidal interpolation provides high-resolution angular position feedback from the motors.

Software has been written to provide communication between the joystick and an external personal computer (PC) through the following interfaces: a standard PC serial port, Universal Serial Bus (USB) ver.1.1, and a standard PC parallel port interface. This communication allows the joystick endpoint position and velocity data to be sent from the joystick to the PC to continuously update a virtual environment and to elicit a force command from the PC virtual environment to the joystick, where it can be felt by the user. The parallel port provided best performance for haptic communication. Testing of the parallel port link between a PC and the second generation x86 based control electronics has confirmed a maximum frame rate of 1.5 kHz (1500 packets of information per second). Since each packet includes 700 bits of data, the data rate to PC is approximately 1 Mbps.

2   Copyright © 2004 by ASME

SPACIAL LINKAGE

For a full derivation of the joystick kinematics, the reader should refer to Adelstein, Ho and Kazerooni [1]. The joystick mechanism consists of two spherical loops and one planar loop. The first loop is composed of links 1, 2, 3, 4 and 5 and the second contains links 5, 6, 7, 8 and 1. (See Fig. 2 for the full linkage assembly and link labeling.) These two loops form a spherical linkage because the axes of all its joints intersect at one common point. The final loop comprising links 4, 5, 6, 10, and 9 form a planar parallelogram structure.

The shape of the links has changed significantly from our previous implementations so as to attain the mass balance and workspace improvements discussed later in this paper, but the relative locations of the revolute joints have not changed. The new linkage is kinematically equivalent to the simplified sketch of the original linkage architecture shown in Fig. 2. One of the most pronounced changes is that the new linkage (Fig. 5) has the end effector inverted such that it is directed in the positive z direction, thereby increasing the usable workspace. Other less visible changes were made to the relative orientation of several links within the spherical portion of the mechanism.

The coordinate system used to describe the linkage kinematics is shown in Fig. 3. The origin is located at the intersection of the three motor shafts. The positive x-axis points into the Γ motor shaft, the positive y-axis points out of the plane of the motor shafts, and the positive z-axis points into the A motor shaft. Positive angle measurements are defined according to the right hand rule about axes pointing from the origin to motors A, B, and Γ. Zero angle measurements are defined as the x-z plane containing the motor shafts.
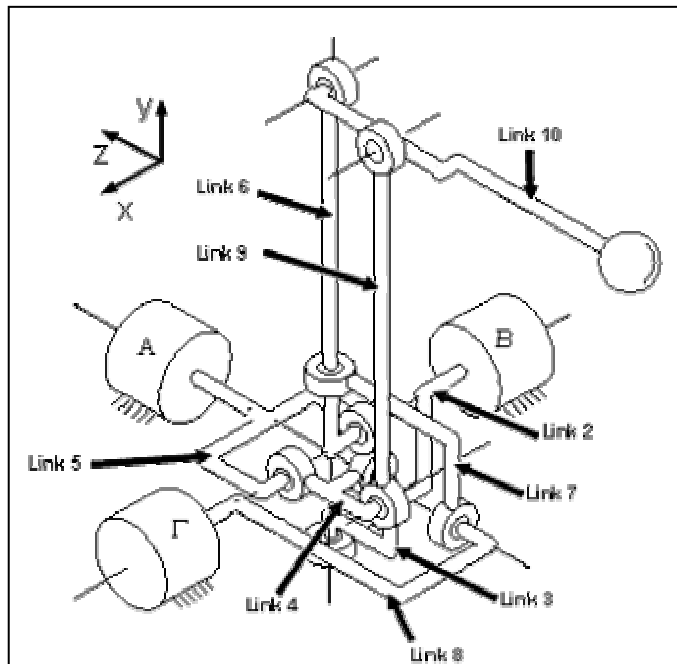
Figure 2: Simplified view of the original joystick linkage from [1]. This configuration is kinematically equivalent to the new linkage design.
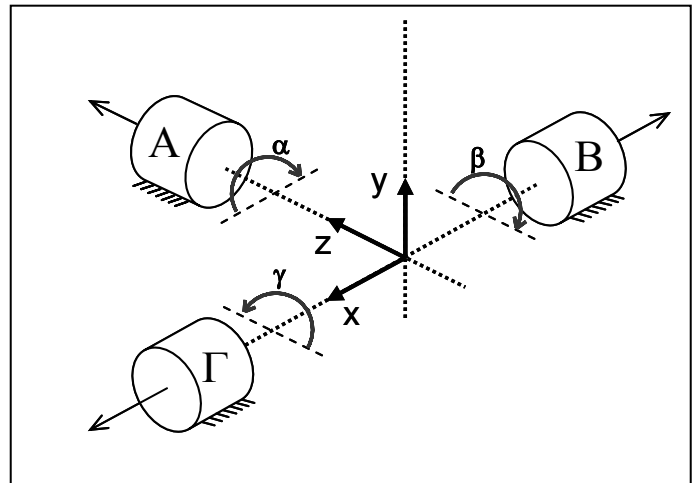
Figure 3: The coordinate system used to describe the joystick linkage kinematics. Positive angular (α, β, and γ) and translational (x, y, and z) displacement are labeled. Actuators are labeled A, B, and Γ. The origin of the xyz coordinate frame is located at the mechanism center of the spherical portion of the linkage.

The derivation of the forward kinematics of the linkage that map the joint angles of the actuators to the Cartesian coordinates of the end effector and the system Jacobian that relates the endpoint force to the actuator torque can be found in [1].

PASSIVE MASS BALANCE

Balancing of the linkage in haptic devices is a technique used extensively in robotics. When implemented, the user does not need to provide a supporting force, imparting a lighter feel to virtual environment simulations [15]. By balancing the linkage passively (as opposed to an active balance that relies on power from the actuators [16]), we are able to reduce computational burden for the embedded processor. The passive balance also allows for a smooth simulation of a zero-force condition in the virtual environment because the actuators can be completely unpowered.

Passive mass balance of the linkages is achieved if the torque induced by gravity, τ_i, for each actuator $(i = 1, ...,3)$ remain at zero. This torque can be defined in terms of the partial derivative of the gravity potential energy of the system with respect to each actuator coordinate. In equation form,

$$\tau_i = \frac{\partial U}{\partial q_i} = 0 \tag{1}$$

where U is the potential energy of the whole system and q_i is the ith system coordinate. Equation (1) will be satisfied if the derivatives of U are forced to be constant for all q_i. The equations for the derivatives of the potential energy, U, are expressed in terms of the mass and location of the mass center for each link and its attached counterweights in the local link coordinate frame and the displacement of the link mass centers above a datum as a function of actuator angles. The mass and center of mass location are specific to the designed set of

3   Copyright © 2004 by ASME

Figure 4: The coordinate system used to define the link dimensions. In this example, D_b is greater than zero and for base links 2, 5, and 8 the origin frame (x_a^*, z_a^*) is at the mechanism center. Link pairs corresponding to *link a* and *link b* in this diagram are 3 and 2, 4 and 5, 6 and 5, and 7 and 8, respectively. For all planar links, L_b is equal to zero.

joystick links. The actuator angles are not dependent on the shapes of the links in the joystick design (given that all designs are kinematically equivalent), but rather on the instantaneous position of the endpoint. The various terms dependent on link mass and center of mass are grouped according to the specific trigonometric functions of actuator angles terms that they multiply. These groupings of link properties become coefficients, which when scaled by gravity acceleration, g, multiply terms that are dependent solely on actuator angle. If each of these coefficients can be driven to zero, the derivatives of the potential energy would be driven to zero, and the potential energy, U, would also be constant. The system would thereafter satisfy the passive mass balance condition expressed by the partial derivative condition of Eq. (1).

The potential energy derivatives, regardless of linkage pose, are defined when the fixed base is aligned perpendicular to the gravity vector, according to the following three equations:

$$\frac{\partial U}{\partial \alpha} = -k_{2y}\, s\alpha + k_{6y}\, c\alpha - k_{7y}\,\frac{c^3\beta\, s\alpha}{d_\beta^3}\ldots$$

$$+ k_{8y}\,\frac{c\alpha\, c^2\beta}{d_\beta^3} - k_{9y}\, s\alpha\, c\alpha\, s\beta\,\frac{c^2\beta + Q_{ab}^2}{d_\beta^3}\ldots$$

$$- k_{10y}\,\frac{c^3\gamma\, s\alpha}{d_\gamma^3} + k_{11y}\,\frac{c\alpha\, c^2\gamma}{d_\gamma^3}\ldots$$

$$- k_{12y}\, s\alpha\, c\alpha\, s\gamma\,\frac{c^2\gamma + Q_{ac}^2}{d_\gamma^3}$$

$$\frac{\partial U}{\partial \beta} = k_{4y}\, c\beta - k_{7y}\,\frac{s\beta\, c^3\alpha}{d_\beta^3} \tag{2}$$

$$\frac{\partial U}{\partial \gamma} = k_{5y}\, c\gamma - k_{10y}\,\frac{s\gamma\, c^3\alpha}{d_\gamma^3} \tag{3}$$

(4)

Where
$$d_\beta = \sqrt{1 - s^2\alpha\, s^2\beta} \tag{5}$$

$$d_\gamma = \sqrt{1 - s^2\alpha\, s^2\gamma} \tag{6}$$

The coefficients used in Eq. (2)–(4) are expanded in Table 1. They are subscripted y to acknowledge the vertical gravity vector as being in the y direction.

k_{1y}	$m_2 g y_2$
k_{2y}	$m_5 g y_5$
k_{3y}	$m_8 g y_8$
k_{4y}	$m_2 g x_2 + m_3 g\,(D_3 + H_2 + z_3)$
k_{5y}	$m_7 g\,(D_7 + H_8 + z_7) + m_8 g x_8$
k_{6y}	$m_4 g\,(D_4 + H_5 + z_4) + m_5 g x_5 + m_6 g\,(D_6 + H_5 + z_6)\mathrm{K} + m_9 g\,(D_4 + D_9 + H_5 + z_9) + m_{10} g\,(D_{10} + D_4 + D_9 + H_5 + z_{10})$
k_{7y}	$m_3 g x_3 + m_4 g x_4 + m_9 g H_{4p} + m_{10} g (X_{10} + H_{4p})$
k_{8y}	$m_3 g y_3$
k_{9y}	$-m_4 g y_4 + m_{10} g y_{10}$
k_{10y}	$-m_6 g x_6 - m_7 g x_7 + m_9 g x_9 + m_{10} g H_9$
k_{11y}	$-m_7 g y_7$
k_{12y}	$m_6 g y_6 - m_9 g y_9$

Table 1: Expanded coefficients of the potential energy

In Table 1, m_i is the mass of the ith link; g is the gravity acceleration; x_i, y_i, and z_i are the coordinates of the center of mass of the ith link measured from the local link coordinate system; and the remaining variables are link dimensions. The link dimension coordinate systems are defined according to Fig. 4.

Seven of the coefficients defined in table 1 are immediately reduced to zero because of the trivial symmetry that occurs when individual link centers of mass are located in the plane of the x-z axes of Fig. 4. (i.e., where $y_i = 0$). This leaves only coefficients k_{4y}, k_{5y}, k_{6y}, k_{7y}, and k_{10y}. Furthermore, a solution to these equations can be shown to guarantee mass balance for all gravity vector orientations even though Eq (2)-(4) are derived for the case where the linkage base is horizontal.

The values of each coefficient were calculated in a spreadsheet as link mass and dimensions and counterweight mass and placement were manually varied in an iterative process to produce the final static balance. In addition, holes

4
Copyright © 2004 by ASME

were bored through the non-counterweight portions of links to decrease the amount of counterweight mass needed and to reduce the overall system inertia. Tests with standard masses confirmed that the maximum vertical force required to support the unpowered linkage for the final designs was less than 0.02 N (2 g) for all endpoint locations tested within the workspace.

With repeated design iterations, the residual force associated with any remaining mass imbalance is negligible in comparison to the bearing friction and other imperfections associated with joint alignment and linkage dimension precision in the actual system. The friction and alignment related forces in the final joystick were insignificant enough that a test user did not feel that her motions were impeded when the machine was unpowered. The mass balance design was considered complete when the unpowered linkage could be released at any position inside the workspace with no resulting movement of the end effector.

The changes that occur as link dimensions were modified to improve mass balance can introduce collisions between links that would decrease the joystick's useable, interference-free workspace. Therefore, as modifications were made, workspace extent was monitored prior to fabrication on the CAD parts using the visualNastran® kinematic simulation package from MSC Corp. The formulation of the mass balance problem is well suited to a numerical optimization approach. However, at the time this research was conducted there was not an easy way to incorporate a workspace analysis into an optimization penalty function and the manual technique described above was expedient and successful. The numerical optimization approach presents an interesting avenue for future research with this hardware. The final result of the mass balance and link redesign provided a larger workspace than did previous versions of the small joystick.

LINKAGE MANUFACTURE

The first linkage (Fig. 5-A) was constructed from polycarbonate plastic parts on a Fused Deposition Modeling (FDM) rapid prototyping system (Stratasys Inc., Model: TITAN) in the laboratory at UC Berkeley. The FDM process allowed for the rapid construction and testing of several prototypes of the linkage. Brass extrusions were chosen as the counterweight material for their density, low cost, and ease of machining. The penalty for using the FDM fabrication process was greater linkage compliance due to the FDM plastic, poorer dimensional tolerance due to the 0.25 mm precision of the FDM machine, and brittleness which made the sections of the links near the bearings and counterweights prone to crack during assembly.
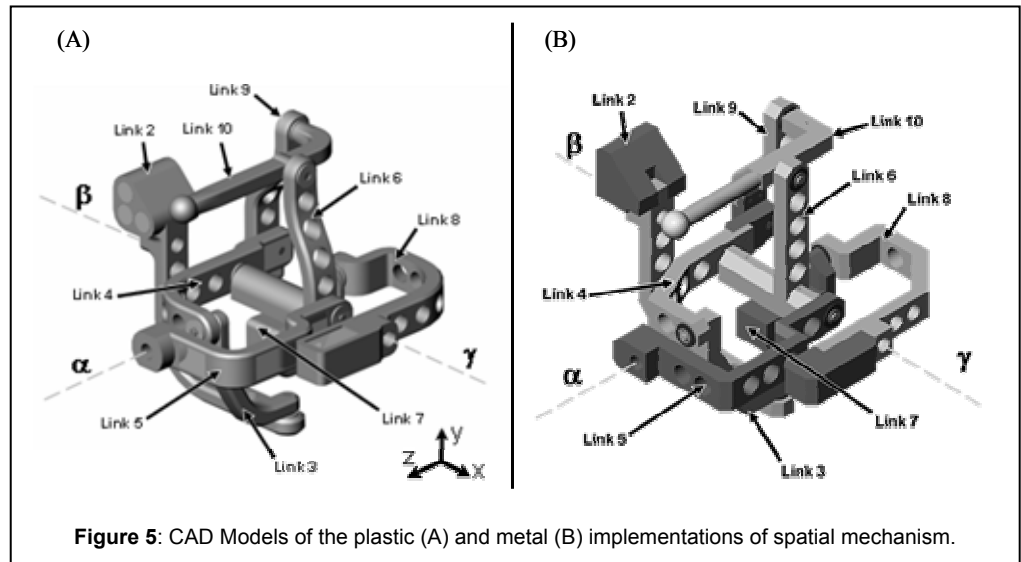
Figure 5: CAD Models of the plastic (A) and metal (B) implementations of spatial mechanism.

In parallel, another version of the linkage (Fig. 5-B) was designed using a combination of 6061-T6 alloy aluminum and 304 alloy stainless steel links. The all-metal construction enabled tolerances significantly better than the 0.25mm of the FDM process. The precision and stiffness of this design make it more suitable for use in the human performance experiments. However, the higher manufacturing cost makes the design less appealing commercially.

Various graspable stylus designs were also created and can be connected to the linkage via a low friction magnetic ball joint that is coupled to the endpoint (at Link 10) of the joystick linkage.

SINUSOIDAL ENCODER INTERPOLATION

Incremental optical encoders measure shaft rotation angles by detecting the motion of a uniform radial grating pattern of alternating transparent and opaque lines arranged around the circumference of disk fixed to the shaft [17]. Typically, a threshold is applied to the output of the sensor detecting the varying light pattern to give a square-wave (high/low) output from the encoder. Encoders usually have two tracks of grating patterns (typically labeled A and B) offset circumferentially from each other by one-quarter of the grating period such that there is a 90° spatial (termed quadrature) phase shift between the two output traces. With two tracks and two possible states per track (high/low), a total of 2 bits of information is available, giving a fourfold increase in encoder resolution over the disk's grating line density. This resolution enhancement and subsequent angle accumulation (i.e., counting of state transitions) is typically carried out by integrated electronic quadrature decoder/counter circuits.

To achieve angular resolution levels well beyond those achievable through quadrature decoding, we use sinusoidal encoders and implement a sinusoidal interpolation scheme. Sinusoidal encoders' mechano-optical components operate like those described above but provide the individual 90° phase-shifted quadrature channels as differentially amplified,
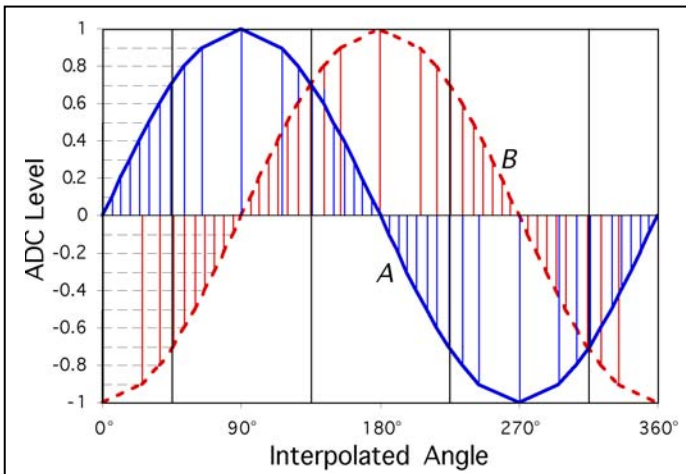
Fig. 6 Nonlinear arcsine mapping of sinusoidal A and B channel quadrature output levels to rotation angle for one encoder line cycle. Equal ADC sample intervals (vertical axis) correspond to non-uniform interpolated angle increments indicated by drop-lines.

continuously-varying analog sinusoid signals, without conversion into two-state digital logic levels.

To compute the interpolation, the continuous channel A and B signals first undergo analog-to-digital (A/D) conversion. A/D conversion of the sinusoids results in digitized signals that are discretized into uniform amplitude increments as depicted schematically in Fig. 6 for operation about a single encoder grating line. Interpolation of the phase angle for each sinusoid — i.e., $\alpha = \arcsin(A)$ and $\beta = \arcsin(B)$ — requires calculation of the inverse sine of each signal. However, because the inverse sine function is a nonlinear mapping, the uniform A/D conversion (ADC) increments yield variable size angle increments. Consequently, interpolated phase angle increments plotted in Fig. 6 show highest density sampling as the sinusoids' amplitudes approach zero from either above or below.

From the overlapping sinusoidal curves in Fig. 6, it is seen that the higher phase angle sample densities span 90° segments that alternate between the two encoder channels A and B. These 90° segments correspond to quarter rotations through individual grating lines equivalent to the conventional encoder quadrature resolution. Thus, by switching every 90° between the two curves whenever they pass through ±0.707 of the peak amplitude, it is possible to maximize the effective angle interpolation resolution across each encoder grating cycle by using only the most densely sampled regions of each inverse sine function.

Because there are a fixed number of discrete sinusoid ADC levels, it is more efficient in practice to retrieve arcsine values from a pre-computed lookup table (LUT) than it is to repeatedly compute on-line floating-point calculations. Additionally, encoding LUT angle entries as fixed-point binary numbers enables the subsequently described interpolation steps to be carried out with simple Boolean operations, further avoiding resource-intensive floating point math. Finally, limiting the size of the LUT helps reduce the amount of

memory required for implementing the interpolation scheme. From Fig. 6, it is noted that the alternating 90° high resolution regions for each channel (A or B) are composed of successive mirrored 45° segments: the first from the sinusoid's negative amplitude portion prior to the zero-crossing, and the second from the positive portion immediately following the zero crossing. Hence, by taking advantage of the signal's sign, the inverse sine LUT theoretically needs only enough storage to correspond with 45° (1/8) of the sine wave.

INTERPOLATION SCHEME INTERPRETATION

The encoders used in both versions of the device discussed in this paper have incremental 1024 line sinusoidal output (Computer Optical Inc.; Model CP-5150). In the first generation device, 8-bit differential A/D converters sample encoder channel A and B voltages, with the ADC output values spanning integers −128 to +127 for the resultant ±1 volt sinusoidal signal inputs. The quadrant of the current encoder position is simply determined from the sign of the ADC value of channel A and B (i.e., by checking the ADC most significant bit), as shown in Fig. 7. As noted above, the signs and therefore the quadrants correspond to the standard encoder quadrature signals.

Within each quadrant, the interpolation input alternates every 45° between the higher resolution segments of channel A and B. For this reason, the LUT only contains values corresponding to positive ADC values between 0 and 90. As seen in Fig. 7, the selection between channels A and B is based on which has the lesser absolute ADC magnitude. Combining the A/B selection with the quadrant information allows computation of the interpolated phase angle between 0° and 360° for the individual encoder line. Thus, the interpolation is composed from 2 bits for the four quadrature quadrants of the 360° cycle, 1 bit for which half of the quadrant is being

sign(A)	−		−		−		+	
sign(B)	−		+		−		−	
Quadrant	I		II		III		IV	
min mag	|B|<|A|	|A|<|B|	|A|<|B|	|B|<|A|	|B|<|A|	|A|<|B|	|A|<|B|	|B|<|A|
offset ± phase	0°+asin(A)	90°−asin(A)	90°+asin(A)	180°−asin(B)	180°+asin(B)	270°−asin(A)	270°+asin(A)	360°−asin(B)
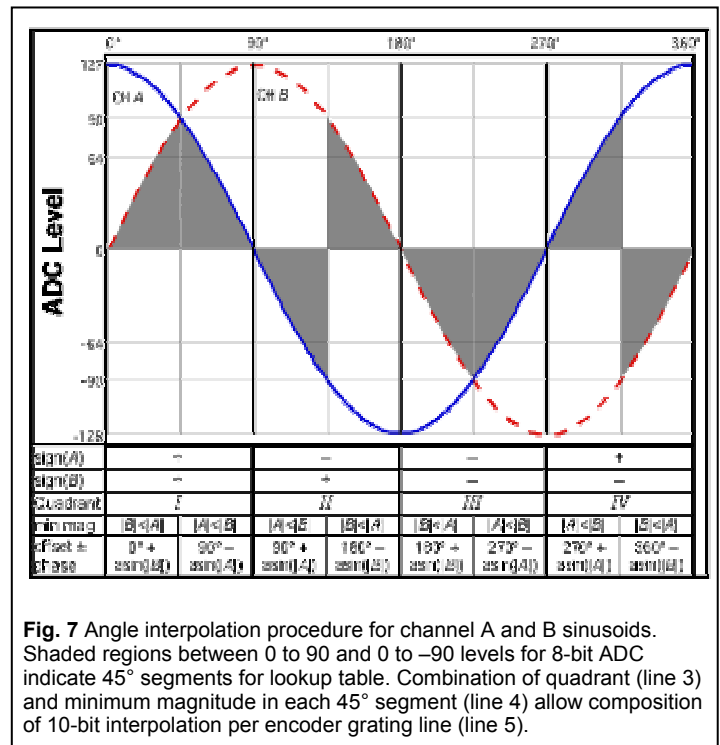
Fig. 7 Angle interpolation procedure for channel A and B sinusoids. Shaded regions between 0 to 90 and 0 to −90 levels for 8-bit ADC indicate 45° segments for lookup table. Combination of quadrant (line 3) and minimum magnitude in each 45° segment (line 4) allow composition of 10-bit interpolation per encoder grating line (line 5).

6   Copyright © 2004 by ASME

interpolated, and a 7-bit LUT density for the 45° segment, for a total of 1024 counts per single encoder grating line. With 1024 lines and 1024 counts per line, the 1024-line encoder produces 1,048,576 counts per revolution. However, as discussed above, some arcsine LUT locations are not addressable by possible ADC levels, resulting in local fluctuations of the interpolation resolution. This degrades the effective resolution to 524,288 counts per revolution, or 0.00069°. At a nominal 10 cm (4 inch) radius for the endpoint of our hand-scale haptic interface, the worst-case sensor resolution corresponds to a theoretical displacement of 1.2μm (4.7×10^{-5} inch), ignoring any possible linkage mechanism compliance, backlash, etc.

INTERPOLATION SCHEME PERFORMANCE

The A/D converters used in our design while rated to 20 MSPS (20 million samples per second), are run at 1 MSPS synchronously with FPGA based quadrature and interpolation circuitry. At 1 MSPS, the ADC and quadrature counters are theoretically capable of capturing all up-down transitions (4 samples/line × 1024 lines) for encoder speeds up to 244.2 rev/s (14.6 KRPM). However, since encoder quadrature in our case is derived from the sign of the sinusoidal signals, the coarse resolution (4 × 1024 counts per revolution) depends solely on each ADC levels' MSB (most significant bit).

Because the interpolation also operates at the 1 MSPS FPGA rate and because the interpolator output is written out to the data bus as a parallel word, full 19-bit high-resolution can be achieved up to the same 14.6 KRPM rotation speeds as the low resolution quadrature count. This performance differs significantly from that expected of the typical 10 to 20X commercially available interpolated encoders. Following the interpolation stage in these commercial sensors, the n-bit wide parallel output is converted back into a dual-track square-wave output so that the resulting quadrature signals can then be decoded and counted by the same interface boards and circuits employed for conventional low resolution (e.g. 1024 line) encoders. Consequently, these commercial devices are limited to operation at slow velocities in order to prevent intervening interpolation level transitions from occurring too quickly to contribute to the pulse pattern. If transitions between adjacent levels are not detected, the pulse train will fail to keep up with shaft rotation and the external quadrature counter circuits will be inaccurate due to the slippage. For example, if our high-resolution output were to be converted back to a quadrature pattern at the full 1 MSPS FPGA rate, counts would be lost if the shaft speed were to exceed 114 RPM (i.e., 1.9 rev/s = 1 MSPS / 524,288 counts/rev).

CUSTOM FPGA BASED INTERPOLATION HARDWARE

We confirmed that quadrature-level resolution could be obtained from the encoder FPGA circuitry at rates far exceeding the minimum 1 kHz target for haptic interface control. The interpolated angle from the FPGA output was displayed via a D/A converter on an oscilloscope. Approximately uniform input velocity produced by connecting a small DC motor to the encoder resulted in the expected sawtooth angle trace (ramp-up until digital value roll-over) that could then be compared with the once-per-revolution encoder index pulse. No slippage between the index pulse and the ramp waveform was noted after several minutes at motor speeds of 150 rev/s (9000 RPM), indicating that the ADC quadrature update, and therefore the high-resolution interpolation output, could be maintained up to rates of 614.4 kHz (150 rev/s × 1024 lines/rev × 4 counts/line).

Experimental validation is currently underway to assess the interpolator's spatial fidelity. Particular interest is given to each grating line's sinusoidal cycle, the interpolations of which are subject to inaccuracies (systematic errors) caused by the sensor's internal electro-optical properties, sensor misalignment at the time of assembly, and imprecise electronic adjustment. These factors can produce nonzero offsets and unmatched or improperly scaled gains for channel A and B encoder output signals, as well as imperfect (non-90°) phasing between the channels. Additionally, the encoder's signals can deviate significantly from the ideal sinusoidal profile [18]. Moreover, the signals' waveform, gain, and offset may also vary from line to line around the circumference of the encoder disk.

Initial observations for our haptic interface's three encoders indicate that signal profiles very closely resemble sinusoids, especially within the 45° segments employed by our interpolation. A preliminary analysis of interpolator fidelity was conducted by examining the deviation of the local angle from the expected best fit to the constant velocity displacement. Systematic departures from the best-fit angle were 0.0027°, 0.0041°, and 0.0027° RMS (0.008°, 0.010°, and 0.0045° at worst case peaks) across individual grating lines for the haptic interface's three encoders—prior to any adjustment of LUT output, or external trimming of raw encoder offsets, gains, and phase. Stochastic variability in interpolation output due to sensor or other system noise typically amounted to ±0.0007° (1/500,000 rev) or less when the interface's servo amplifiers and actuators were not powered.

COTS BASED INTERPOLATION HARDWARE

In the second generation device, commercially available encoder interpolation modules were substituted for the custom hardware and software described above in the interest of lowering the cost and increasing the robustness of the system. A standalone encoder interpolator module (Computer Optical Inc.; Model CP-1064-16-1) was added between each encoder and the embedded control computer. The module performs 16X sine interpolation and outputs a standard quadrature signal. With this sine interpolation, and 4X quadrature decoding, the angular position resolution information is 1024x16x4 ≈ 65.5K counts/rev. At the joystick endpoint's maximum reach of 10 cm, this corresponds to a theoretical resolution in *x-y-z* endpoint space of 9.6μm. The actual resolution of the endpoint position is coarser due to factors such as compliance of the links and joints.

MOTORS AND COMMUTATION

Both designs share the same brushless DC motors (BLDC) for actuation (Pittman Motors; ELCOM Model 4141). The motors have four-pole, three-phase slotless sinusoidal

Copyright © 2004 by ASME

windings. The absence of brush-rotor contact in BLDC drives eliminates a source of shaft friction and is therefore beneficial to the "feel" of haptic interface hardware. Most importantly, we employ BLDC motors in our haptic devices because of their higher continuous and peak torque output per unit of actuator size or mass.

The motors were chosen with sinusoidal windings because they provide a constant torque profile when commutated sinusoidally, thus eliminating torque ripple which would be transmitted to the user and would degrade the haptic simulation. At its rated continuous torque, the motor produces approximately 1.4 N (measured) at the end effector when the linkage is fully extended to its maximum 10 cm reach. This force level is sufficient to cover the majority of precision finger-scale manipulation tasks [3]. In addition, a peak force of 5 N can be applied for durations less than 2 seconds (duration limited by the amplifiers).

Commercial pulse width modulated (PWM) servo amplifiers were selected for the haptic interface because of their higher power efficiency and consequent lower heat losses than linear amplifiers. The compact sinusoidal PWM amplifiers (Advanced Motion Controls; Model S16A8) provide a maximum 8A of current per motor (or 75 W per motor based on the motor winding resistance). The PWM amplifiers switching frequency is 33 kHz, well beyond the 20 kHz human audible range and beyond the mechanical bandwidth of the system. The three motors and amplifiers are contained within the desktop joystick housing. The top and bottom plate, onto which the motors and amplifiers are respectively mounted, also serve as heat sinks.

Proper commutation of motor windings, i.e., the energizing of winding phases in the correct sequence, depends on knowledge of the instantaneous angular displacement between rotor and stator. Brushed drives, by design, ensure that the simple mechanical "switching" of the brushes between the rotating commutator bars will always activate the correct phases with respect to the permanent magnet field, without need for additional sensor feedback. In BLDC drives, there is no such direct mechanical connection to account for the angular rotation between rotor magnets and stator windings. Thus, trapezoidal and sinusoidal commutation, the most widely used commutation schemes for BLDC machines, depend on motor shaft angle sensors for this information.

TRAPEZOIDAL COMMUTATION

In trapezoidal commutation, Hall Effect sensors are used to detect the orientation of the rotor magnetic field. Typically, three Hall Effect sensors are distributed around the stator circumference to match the 120° electrical offset between the three winding phases. The two-state signal transitions from the

three Hall sensors serve to divide the rotation into unique 60° wide segments for each motor magnetic pole pair. Switching logic under direct control of the Hall Effect sensor states will direct current among the trapezoidal amplifier's three output channels to produce the six-step four-level delta-connected winding current profiles depicted in Fig. 8. This straightforward current switching strategy makes trapezoidal (sometime called "six-step", or "brushless DC") servo amplifiers and sensors simpler, less expensive, and, therefore, the more popular of the brushless commutation techniques.
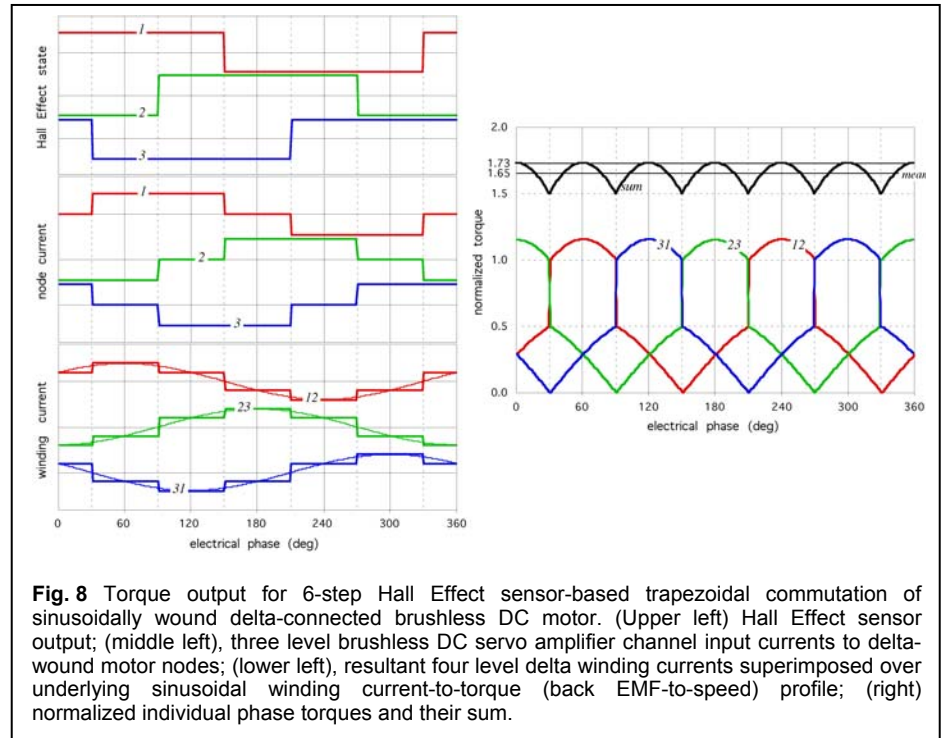
Fig. 8 Torque output for 6-step Hall Effect sensor-based trapezoidal commutation of sinusoidally wound delta-connected brushless DC motor. (Upper left) Hall Effect sensor output; (middle left), three level brushless DC servo amplifier channel input currents to delta-wound motor nodes; (lower left), resultant four level delta winding currents superimposed over underlying sinusoidal winding current-to-torque (back EMF-to-speed) profile; (right) normalized individual phase torques and their sum.

Both a motor's back EMF (i.e., generator voltage) pattern in relation to uniform velocity and the relation of torque profile to constant drive current depend on the design and construction of its winding coils and permanent magnets. Specifically, sinusoidal windings generate sinusoidal torque patterns in response to constant current. Consequently, the application of trapezoidal commutation currents that are not matched to sinusoidal winding torque profile induces spatially periodic deviations from commanded actuator torque, termed "ripple." As illustrated in Fig. 8 for the six-step commutation of sinusoidally wound, delta-connected BLDC machines, the theoretical peak-to-peak ripple is 13.4% of the highest torque— a level that is unacceptably palpable to the haptic interface user. (Note that related current patterns produce the same 13.4% torque ripple for the alternative wye-connected BLDC motor windings.). With six transitions per electrical period (i.e., per permanent magnet pole pair) occurring while commutated current levels abruptly switch, the torque ripple cycle would repeat twelve times per shaft rotation, or every 30°, for our hand-scale device's four-pole motors.

8   Copyright © 2004 by ASME
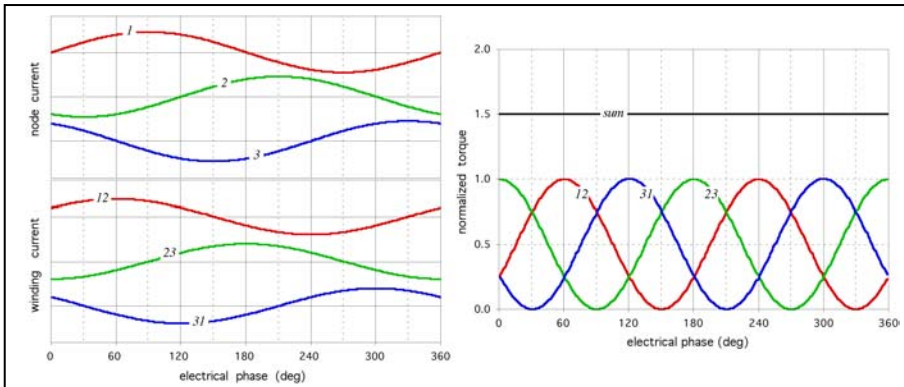
Fig. 9 Torque output for sinusoidal commutation of sinusoidally wound delta-connected brushless DC motor. (Upper left) sinusoidal brushless AC servo amplifier channel input currents to delta-wound motor nodes; (lower left) resultant sinusoidal winding currents coincident with underlying sinusoidal winding current-to-torque (back EMF-to-speed) profile; (right) normalized sum and individual phase torques.

SINUSOIDAL COMMUTATION

From Fig. 8, we see that the torque ripple arising from trapezoidal commutation coincides with significant departures in winding currents from the underlying sinusoidal current-to-torque (or back EMF) profile. Essentially, the BLDC motor ripple is caused by the four-level switched waveform's overly coarse sinusoid approximation, and can therefore be remedied by refining the commutation profile.

Ideally, by matching individual phase currents to the particular motor winding's spatial and temporal torque characteristics, sinusoidal commutation can completely eliminate torque ripple as shown in Fig. 9. However, as noted from Figs. 8 and 9, a perfectly matched sinusoidal (also called "AC brushless") amplifier will reduce mean torque to ~91% (i.e., 1.5 / 1.65) of that obtainable with trapezoidal commutation for a given sinusoidally wound BLDC motor.

Depending on the particular servo amplifier design, either encoders with direct angular output or resolvers that automatically convert angle to commutation-ready sinusoidal waveforms are typically required to provide the necessary rotation feedback for sinusoidal commutation. In our haptic interface, we employ the incremental encoders described above in conjunction with the appropriate three-phase servo amplifiers.

Unlike resolvers, which measure absolute rotation permanently referenced to stator orientation, incremental rotary encoders report angle relative to the quadrature counter's last initialization. Encoder angle may be referenced to the BLDC motor winding phases by several methods. Without resorting to secondary absolute rotation sensors, the encoder can be installed on the motor such that its index channel (an optional third disk track with only a single grating line) produces a pulse when crossing a single predetermined winding location. This location would, for example, coincide with the shaft angle of a Hall Effect transition shown in Fig. 8, if such a secondary rotation sensor were present. The encoder counter would be initialized upon the first index pulse crossing and would from

then on be able to indicate the rotor relative commutation phasing.

Alternatively, once the index pulse is placed, absolute shaft angles for a unique pre-specified joystick linkage pose can be measured and recorded. Provided that the a method exists for locating the linkage in this reference pose for subsequent restarts, the encoders' initial angular offsets will be the known pre-recorded starting pose angles. Thus commutation could be initiated without first seeking out each encoder's index pulse or specified Hall Effect transitions.

The amplifiers themselves do not produce the sinusoidal commutation pattern; it is instead generated on board the low-level control electronics. Each servo amplifier simply takes in a pair of control signals (presumed to be phased 120° apart) that already incorporate the modulation of the desired torque command by the commutation profile, and produces three-channel PWM current output. Two of the amplifier output channels directly follow the input control phases. The amplifier derives the third phase internally under the assumption that the three channels' instantaneous currents sum to zero. Because the low-level control is software configurable, six-step or other balanced non-sinusoidal commutation patterns may also be implemented on the amplifiers.

IMPLEMENTATION OF CUSTOM FPGA BASED COMMUTATION

The modulation of the commanded input torque by the respective windings' commutation profile entails real-time multiplication on the FPGA of the torque command by the appropriate angle-dependent sinusoidal levels. The commutation profile, pre-computed for equally spaced angle intervals, is stored on the FPGA as a single 256-point sine curve LUT. Though the LUT only covers the first quarter commutation cycle (0° to 90°), the same sine values can also be used for the remainder of the cycle—either directly (from 90° to 180°) or with a sign inversion (180° to 360°). Moreover, to span the entire 10-bit commutation cycle ($2^{10} = 4 \times 256$ points per segment), only the 11 most significant (two electrical cycles per mechanical revolution) bits of the interpolated encoder reading are required to address LUT angle entries.

The modulation process proceeds in the following order. First, prior to addressing the sine LUT, the encoder angles are adjusted for offsets between the initializing index pulse and the individual 120°-shifted winding phase orientations. Second, sine LUT output values for the offset-adjusted angles are then multiplied by the torque command. Finally, the two 120° shifted control signal channels resulting from the multiplication (i.e., the commutation-modulated torque commands) are issued via a pair of bipolar 14-bit digital-to-analog converters (DACs) to each servo amplifier. Since there is only one LUT for this process that is shared by the haptic interface's three motors, the sinusoidal profile cannot be applied simultaneously to each of

9   Copyright © 2004 by ASME

the amplifier input channels. Instead, there is a 2 μs time skewing between the loading of successive DAC channels, contributing to a cumulative six channel latency of 12 μs (6 × 2 μs). The individual DAC's 16 μs settling time, which limits the maximum commutation update rate, but is long enough that the commutation cycle is not further slowed by the accumulated inter-channel delay. The resulting 62 kHz FPGA commutation update rate is still nearly double the commercial servo amplifiers' nominal 33 kHz PWM switching frequency.

Subjectively, we observed that the implementation of sinusoidally commutation in our hand-scale haptic device has eliminated any perceptible evidence of ripple, which had been significant under the prior trapezoidal commutation at 30° intervals. We have not yet attempted formal calibration of the new motor and consequent overall haptic interface dynamics under the improvements afforded by the sinusoidal drives.

DSP/FPGA BASED CONTROL HARDWARE

The DSP/FPGA based control electronics used an embedded DSP based controller (Innovative Integration, Model: SBC6x) to perform what we refer to as mid-level functions: kinematic transformations, closed-loop servo-motor control, workspace boundary enforcement, and active mass counterbalance. In addition, the embedded controller managed either USB or serial communication with a PC running a virtual environment (we refer to this as high-level control). Low-level control, which included encoder interpolation, velocity derivation through a digital filter, and servo-motor commutation, was performed by a custom-designed add-on board that attaches to the embedded DSP controller. The add-on board contained the FPGA for performing these functions as well as analog-to-digital converters (ADC), digital-to-analog converters (DAC), and signal conditioning hardware for sampling encoders and outputting motor commands. The FPGA allowed many functions to be integrated into a single chip and, because the FPGA can be reprogrammed, provided a flexible platform for experimentation and debugging. While this custom-hardware control system for the joystick performed adequately in the original prototype, it was both difficult and expensive to duplicate in the laboratory due to noise and signal integrity issues on the custom FPGA add-on board and the fact that the all surface-mount component design made in-house assembly impractical. While we feel the FPGA based architecture would be a logical choice for a production version of the joystick, the decision was made to switch to a COTS control hardware architecture to reduce the cost for future prototypes and create a more rugged/reliable experimentation platform for use in the lab.

Figure 10: Control hardware and software architecture.

IMPLEMENTATION OF COTS BASED COMMUTATION

In this latest generation of control electronics, sinusoidal commutation is handled automatically by a motion control daughter-card for the embedded microprocessor. The features and capability of the motion control card is discussed in greater detail in the description of the Commercially available Off-The-Shelf (COTS) system in the following section.

JOYSTICK CONTROL ELECTRONICS

The system hardware consists of high, mid, and low level control electronics and physical interface components consisting of the linkage, motors and power amplifiers, optical encoders and sinusoidal encoder interpolators as shown in Fig 10. In the original custom control electronics design, Mid-level control was implemented on a DSP board and low-level on an FPGA board. The second generation control electronics used an embedded x86 processor board for mid-level control and a motion processor daughter board for low-level control.

COTS CONTROL HARDWARE

The control architecture for the latest generation haptic joystick shares the same low--mid-high level control division as the DSP/FPGA version, however we have chosen different approaches for each to make an all off-the-shelf system and reduce cost significantly. Mid-level control is now managed by an embedded x86 based microprocessor and the combination of a dedicated motion control chip and an encoder interpolation module take care of low-level functions. Together, they form the stand-alone controller that is housed inside the joystick base enclosure along with the motors and servo amplifiers.

The mid-level control is performed by the embedded Intel 386EX microprocessor on a development board from Tern Inc. (Model: i386-Engine). The mid-level board is responsible for the servo control function that calculates the commanded interaction forces as well as the workspace boundary

10   Copyright © 2004 by ASME

enforcement function that prevents motion into regions where link interference would occur. The mid-level control also includes a parallel communication interface to an optional external computer that can run virtual environment simulations.

The low level control is carried out on the Tern MotionC-S development board with PMD Navigator® Series motion processor. The motion processor performs quadrature decoding to give angular position for each axis. It also estimates velocity by keeping track of the number of encoder counts over a known time window. The low-level embedded controller can vary the size of this window to improve the velocity estimate for slow motions. The PMD chip is also responsible for the sinusoidal motor commutation.

SOFTWARE

The joystick appears to the user as an impedance-controlled device. Under impedance control, the input is the motion of the endpoint generated by the human. This motion is sensed by the device's encoders and transformed to motion of a virtual endpoint in a virtual environment running on the either on the embedded processor or an external personal computer. The output signal (feedback) to the user is the point force generated by the joystick at its end effector. Our device is intended to interface with existing virtual environment software for the PC. This virtual environment software determines what force should be generated at the end effector based on its location in the virtual environment. For example, if the end effector in the virtual environment were to strike a virtual "wall," a force proportional to the depth of penetration of the virtual wall could be generated. We also developed a simple API for the haptic device controller to interface with the PC virtual environment software. The API includes functions to obtain the end effector position and velocity, and can output a three-component force vector at end effector force. This way the virtual environment developer can utilize the API to create new Microsoft Windows applications that incorporate the relationship that best fits the experiment or haptic environment he or she is trying to create.

The software architecture is shown in Fig. 10. The local (mid-level) processor converts the encoder counts for each actuator axis into angle measurements. The forward kinematic relations are then applied to obtain the end effector position and velocity in Cartesian coordinates. The state of the end effector is made available to the external PC running the virtual environment through the API. Based on this information, the external PC determines the appropriate force in Cartesian coordinates to apply at the end effector. It then sends this out to the local processor through the API, and the user is given the option to command the forces directly (and close the loop on the external PC) or use a PID based impedance control running on the embedded processor. In either case, the force command is converted into actuator torques using the instantaneous Jacobian and sent out to the actuators. The local processor also performs workspace boundary enforcement in the actuator angle coordinate space by placing virtual haptic "walls" near the boundaries of the physical workspace to prevent the user from colliding the linkage into itself or the device housing.

Convincing haptic simulations are widely reported to require update rates in excess of 1 kHz [19]. The local haptic environment running on the embedded microprocessor can be updated at a rate of up to 1.5 kHz. If other haptic calculations are occurring on the PC, the endpoint position and velocity and force command data must be transferred at 1 kHz between the PC and local microprocessor.

The DSP/FPGA version of the haptic joystick relied on either an RS232 serial or USB ver.1.1 communication link with the VE. The serial link was limited to the maximum PC serial port speed of 115.2 kbps. While USB has become a standard high-speed interface for PCs and seems like a promising technology for haptic communication, it does so by transmitting large blocks of data at a fairly slow rate: a maximum of 500 Hz. for USB 1.1 [20]. The new USB 2.0 standard, with a frame rate eight times higher than USB 1.1, was not available at the time our system was developed. In the COTS control hardware version of the joystick, a standard high speed PC parallel port is used and a 1 kHz frame rate, 1 Mbps data transfer rate connection was established between the PC and the haptic device. While sufficient for a convincing haptic simulation, the data rate is intentionally made less than the maximum achieved in testing to guarantee performance in the Windows PC environment.

CONCLUSIONS

We have designed a three-degree-of-freedom force-feedback haptic joystick with the goal of combining portability and compact size with the performance, spatial resolution, continuous force magnitude, smoothness, balance, and haptic update rate necessary for precision finger-based interaction. The current iteration of the joystick uses links kinematically equivalent to past versions. However, the new design provides a larger workspace and is passively mass balanced.

Two versions of the mechanical linkage were prototyped: a low cost FDM polycarbonate linkage potentially suitable for mass production and a precision all-metal linkage designed for haptics research. However, because of dimensional imprecision and excessive compliance, further development of the FDM version has been postponed for now. Sinusoidal encoder interpolation and sinusoidal motor commutation have been implemented to achieve high resolution, smooth haptic simulation.

Software has been written to allow for high-speed data transfers between the joystick and the PC, and a simple API is also provided to allow the haptic device to interact with other virtual environment software. The DSP/FGPA based control electronics design has been completed and tested. The function of individual device subsystems for the COTS based control electronics design have thus far been tested separately. For this latest generation of the device, we expect shortly to begin the process of integrating the communication software and API with the low-level control code on the embedded platform and connect the control system to the actuated linkage. Testing of the completed hardware and software system for the COTS system will follow.

Copyright © 2004 by ASME

NOMENCLATURE

Abbreviations:

API	Application Program Interface
BLDC	Brushless DC (type of electric motor)
CAD	Computer Aided Design
COTS	Commercially available Off-The-Shelf components
dpi	Dots per inch
FDM	Fused Deposition Modeling
PC	Personal Computer
PID	Controller with output proportional to the error, the error integral, and the error derivative
TTL	Transistor-Transistor Logic (digital signal standard)
USB	Universal Serial Bus
VE	Virtual Environment
kbps	Thousand bits per second (data transfer rate)
x86	Generic name for a series of Intel processors

Variables Used in Paper:

D_b	Link thickness (see Fig. 4)
H_b	Offset along x_b axis between revolute joints on a link (see Fig. 4)
J	Instantaneous Jacobian of the spatial linkage
K_{ny}	n^{th} coefficient of the potential energy derivative equations for the linkage (includes link mass and geometry terms but no orientation dependant terms). The y subscript denotes only components of potential energy in y direction.
L_b	Offset along the x_b^* axis between revolute joints on a link (see Fig. 4)
U	Linkage potential energy
cn, sn	Cos(n) and Sin(n)
x, y, z	Cartesian end effector coordinates
x_b, z_b	Coordinate axes associated with the first revolute joint encountered on a link when progressing from a lower numbered link to a higher numbered link in the chain (see Fig. 4).
x_b^*, z_b^*	Coordinate axes associated with the second revolute joint encountered on a link when progressing from a lower numbered link to a higher numbered link in the chain (see Fig. 4).
A, B, Γ	Three DC motor actuators in the haptic device
α, β, γ	Axes associated with actuators $A, B,$ and $\Gamma,$ also represents angle of actuator rotation for each axis

REFERENCES

[1] Adelstein, B.D., Ho, P., and Kazerooni, H., 1996, "Kinematic design of a three degree of freedom parallel hand controller mechanism," *Proc. 5th Symposium on Haptic Interfaces for Virtual Environment and Teleoperator Systems, ASME Dynamic Systems and Control Division,* DSC-Vol. 58, New York, pp. 539-546.

[2] Millman, P.A., and Colgate, J.E., 1991, "Design of a four degree-of-freedom force reflecting manipulandum with a specified force/torque workspace," *Proc. IEEE Conference on Robotics and Automation,* Sacramento, pp. 1488-1493.

[3] Adelstein, B. D., 1998, "Three degree of freedom parallel mechanical linkage," U.S. Patent No. 5,816,105.

[4] Massie, T. H., and Salisbury, J.K., 1994, "The PHANToM haptic interface: a device for probing virtual objects," *Symposium on Haptic Interfaces for Virtual Environment and Teleoperator Systems, Proc. ASME Dynamic Systems and Control Division*, DSC-Vol. 55-1, New York, pp. 295-301.

[5] Siva, K.V., Dumbreck, A. A., Fischer, P. J., and Abel, E., 1988, "Development of a general purpose hand controller for advanced teleoperation," *Proc. International Symposium on Teleoperation and Control*, Bristol, pp. 277-290.

[6] Brandt, G., Aimlong, A., Carrat, L., Merloz, P., Staudte, H. W., Lavallee, S., Radermacher, K., and Rau, G., 1999, "CIRGOS: a compact robot for image guided orthopedic interventions," *IEEE Transactions on Information Technology in Biomedicine*, Vol. 3-4, pp. 252-260.

[7] Grange, S., Conti, F., Helmer, P., Rouiller, P., and Baur, C., 2001, "Overview of the Delta Haptic Device (poster)," *Eurohaptics 2001*, Birmingham, England.

[8] Melchiorri, C., Vassura, G., and Arcara, P., 1999, "What kind of haptic perception can you get with a

one-wire interface?," *Proc. IEEE Conference on Robotics and Automation,* Detroit, pp. 1620-1625.

[9] Takeda, Y., and Funabashi, H., 2000, "Kinematic synthesis of spatial in-parallel wire-driven mechanism with six degrees of freedom with high force transmissibility," *Proc. ASME 2000 Design Engineering Technical Conferences,* Baltimore, pp. 1-9.

[10] Kim, S., Ishii, M., Koike, Y., and Sato, M., 2000, "Development of tension Based haptic interface and possibility of its application to virtual reality," *Proc. ACM Symposium on Virtual Reality Software and Technology*, pp. 199-205.

[11] Birglen, L., Gosselin, C., Pouliot, N., and Monsarrat, B., 2002, "SHaDe, A new 3-DOF haptic device," *IEEE Transactions on Robotics and Automation,* Vol. 18-2, pp. 166-175.

[12] Ho, P., 2002, "Haptic simulation of 3D primitive objects and textures using a novel force-reflecting interface," Ph.D. Thesis, University of California, Berkeley, Berkeley, CA.

[13] Adelstein, B. D., Gayme, D. F., Kazerooni, H., and Ho, P., 1998, "Three degree of freedom haptic Interface for precision manipulation," *Proc. ASME Dynamic Systems and Control Division*, DSC-Vol. 64, New York, p. 185.

[14] Ho, P., Adelstein, B. D., and Kazerooni, H., 2004, "Judging 2D versus 3D square-wave virtual gratings", *Proceedings,. 12th International Symposium on Haptic Interfaces for Virtual Environment and Teleoperator Systems*, IEEE, Chicago, pp. 176-183.

[15] Ebert-Uphoff, I., Gosselin, C. M., and Laliberte, T., 2000, "Static balancing of spatial parallel platform mechanisms – revisited," *ASME J. Mech. Des.*, Vol. 122, pp. 43-51.

[16] Yu, Y., and Lin, J., 2003, "Active balancing of a flexible linkage with redundant drives," *ASME J. Mech. Des.*, Vol. 125, pp. 119-123.

[17] Slocum, A.H. (1992). *Precision Machine Design*. Prentice Hall: Englewood Cliffs, NJ.

[18] Venema, S., & Hannford, H. (1995). Kalman filter based calibration of precision motion control. *Proceedings, IEEE/RSJ Conference on Intelligent Robots and Systems 95*, Pittsburgh, PA., Vol. 2, pp. 224-229.

[19] Marcus, C. E., 1998, "Force feedback for surgical simulation" *Proc. IEEE,* Vol. 86, pp.524-530.

[20] Anderson, D., 2001, *Universal Serial Bus System Architecture*, 2nd ed., K. Tibbetts, eds., pp. 13-24.